Pacific Northwest
NATIONAL LABORATORY

PNNL-31996

A Radiation-Shielded, Shallow Underground, Long-Coherence Time Quantum Qubit Concept

September 2021

Ben Loer
Brian Archambault
Erin Fuller
Bruce Pierson

U.S. DEPARTMENT OF ENERGY

Prepared for the U.S. Department of Energy
under Contract DE-AC05-76RL01830

DISCLAIMER

PACIFIC NORTHWEST NATIONAL LABORATORY
operated by
BATTELLE
for the
UNITED STATES DEPARTMENT OF ENERGY
under Contract DE-AC05-76RL01830

Printed in the United States of America

Available to DOE and DOE contractors from the
Office of Scientific and Technical Information,
P.O. Box 62, Oak Ridge, TN 37831-0062;
ph: (865) 576-8401
fax: (865) 576-5728
email: reports@adonis.osti.gov

Available to the public from the National Technical Information Service
5301 Shawnee Rd., Alexandria, VA 22312
ph: (800) 553-NTIS (6847)
email: orders@ntis.gov <https://www.ntis.gov/about>
Online ordering: http://www.ntis.gov

PNNL-31996

A Radiation-Shielded, Shallow Underground, Long-Coherence Time Quantum Qubit Concept

September 2021

Ben Loer
Brian Archambault
Erin Fuller
Bruce Pierson

Prepared for
the U.S. Department of Energy
under Contract DE-AC05-76RL01830

Pacific Northwest National Laboratory
Richland, Washington 99354

Abstract

Ionizing radiation from ambient radioactivity has been shown to reduce the coherence time of superconducting qubits. Qubit performance can be improved by shielding the system from external radiation: operating the system underground to reduce cosmic rays, and use of lead shielding to reduce ambient gammas. Here we present a design for a lead shield optimized for a dilution refrigerator operating in PNNL's Shallow Underground Laboratory. The shield reduces the ambient gamma flux by approximately 99.8%, so that cosmic ray muons dominate the ionizing radiation input to the qubits.

1 Introduction

Quantum technologies exploiting entanglement between multiple sensors or computing elements (qubits) have the potential to dramatically improve capability for a subset of computing and sensing applications [1]–[5]. Many different technologies are being investigated for the physical implementation of qubits, but much focus has been placed on superconducting qubits, due primarily to their ease of manufacture with standard semiconductor fabrication techniques and control and readout with microwave pulses [6]–[8]. A key characteristic of qubits affecting their real-world computing potential is the coherence time—how long on average a qubit will remain in a given quantum state. Improving coherence time of superconducting qubits has been a major research focus for the past several years [8].

One source of qubit decoherence is the presence of excess, non-thermal "quasiparticles" (unbound electrons in the superconductor bulk from broken Cooper pairs). Excess quasiparticle densities have been universally observed in nearly all superconducting devices [9]–[12]. Recent experiments have demonstrated that ionizing radiation can directly lead to superconducting qubit decoherence, presumably via quasiparticle generation [13]. If recent trends in improving coherence times continue, typical background levels of radioactivity in the environment will become the leading source of qubit decoherence within ten years. Perhaps even worse, radiation-induced qubit errors are correlated in time across whole device substrates [14]–[16]. This will preclude the majority of quantum error correction techniques, which rely on individual errors to be random and uncorrelated [17]–[20]

In this report, we present a design for a radiation-shielded dilution refrigerator, allowing operation of superconducting qubits with reduced radiation effects. Although such a system may not be practical for large-scale quantum computing systems, it will create a unique opportunity for research into radiation effects in a controlled environment, and studying long-coherence-time qubits absent radiation-induced decoherence. With sufficiently long coherence-time qubits, the residual correlated error bursts from radiation may be manageable by detecting and "vetoing" likely error states with classical sensors [21].

In order to reduce the impact of cosmic ray secondary particles, the shielded facility must be located underground. Ambient gamma radiation from normal laboratory construction materials is attenuated by lead shielding surrounding the dilution refrigerator. The residual cosmic ray-induced radiation rate determines the required effectiveness of the gamma shielding—once the gamma-induced radiation rate is subdominant to cosmic rays, there is very little utility in adding additional lead shielding. In this report, we present a shield optimized for installation in PNNL's Shallow Underground Laboratory (SUL), with a 19 meter earth overburden [22]. We begin by developing a model for the cosmic ray and gamma fluxes in the SUL normalized to *in situ* measurements. We then model these fluxes and a simplified dilution refrigerator containing qubit chips with the `GEANT4` Monte Carlo toolkit [23] to estimate the interaction rate and radiation dose received by the qubits with varying shield designs. Finally we present an engineering model of the lead shielding that accommodates the dilution refrigerator's frame, piping and cabling, and allows access to the experiment space.

2 Methods

2.1 Determining the Radiation Environment

The first step to designing the radiation shield is to determine the background radiation environment in the shallow underground laboratory and how that radiation interacts with the cold target devices. We consider cosmic ray secondaries (muons) and gammas from decay of trace levels of radioactive material in the surrounding environment. The cosmic ray muon flux is attenuated by the overburden of the shallow underground site, but cannot be significantly further attenuated by shielding. Therefore the interaction rate from cosmic rays sets the achievable total event rate, and the radiation shield must reduce the rate from the ambient gamma flux to a small fraction thereof. In Section C we will also consider radioactive emissions from sources inside the dilution refrigerator, but these do not drive the design of the shield.

The cosmic ray flux depends strongly on the height of the overburden, and the ambient gamma flux depends weakly on the materials used to construct the facility. Both the cosmic ray and ambient gamma fluxes are estimated by simulations normalized to measurements. Simulations were performed using the `GEANT4` Monte Carlo toolkit [23]. The laboratory considered was a simplified model of PNNL's shallow underground laboratory (SUL) [22]. The simulated lab consists of a single room, 8 m by 8 m by 4 m high, surrounded by 1.2 m thick concrete walls and a 19 m overburden (above and extending on all sides) composed of calcium carbonate (e.g. limestone). The simulation geometry is shown in Figure 10. Most importantly for real-world comparisons, the simplified model does not include any vertical access shafts, near which there is significantly higher muon flux.

2.1.1 Cosmic rays

Any model estimate of the muon energy deposition rate must be calibrated against experimental reference data to ensure that assumptions used to simplify the model do not impact the results. For this study, spectra acquired from polyvinyl toluene (PVT) scintillation panels placed atop radiation detection systems for use as cosmic muon vetos at ground level and in the SUL were modeled and compared to the measured spectra. Details of the surface simulation comparison are provided in Section A, the remainder of this section is devoted to discussion regarding the simulation and measurement comparison results obtained in the SUL.

The simulated PVT panel the center of the $8 \times 8 \times 4$ m^3 underground volume, 2.4 m from the floor. The energy deposition from `CRY`-generated cosmic particles in a $76 \times 76 \times 5$ cm^3 PVT panel were tallied and normalized to counts per second using the livetime reported by `CRY`. The predicted energy spectrum from Geant4 was compared to the measured spectrum from an equivalent panel operating in the SUL as a cosmic veto for a lead-shielded gas proportional counter in Figure 1. This simulation neglected the large lead mass sitting immediately below the PVT panel and was located more centrally in the lab relative to the actual veto panel, which sat near the concrete walls of the SUL. These liberties were taken with the assumption that additional particles produced by muons in the concrete walls and lead shielding underneath the panel were small relative to the downward muon flux and uncertainties in the simulated spectrum and the material composition of the overburden.

To best fit the measured data, the simulated spectrum is scaled by a factor of 0.7; i.e., the simulation is overestimating the cosmic ray flux by $\sim 30\%$. Good agreement is obtained between the measured and simulated muon peaks, but some discrepancies are observed in the low- and high-energy regions. The discrepancies below the muon peak were anticipated as the terrestrial radiation background source was not included.The asymmetry in the high energy region was not anticipated. However, the integral magnitude of the difference above the primary muon peak is $<1\%$ of the total energy deposited in the PVT panel. Thus, while these deviations between data and model are evident, they are irrelevant to the total energy deposition validation needed for this study. A simulation was conducted of the underground laboratory and doubling the soil density. The integral tally in the PVT panel was reduced by a factor of 2.8 indicating variations in soil density alone could explain the observed disparity between measured and modeled data.

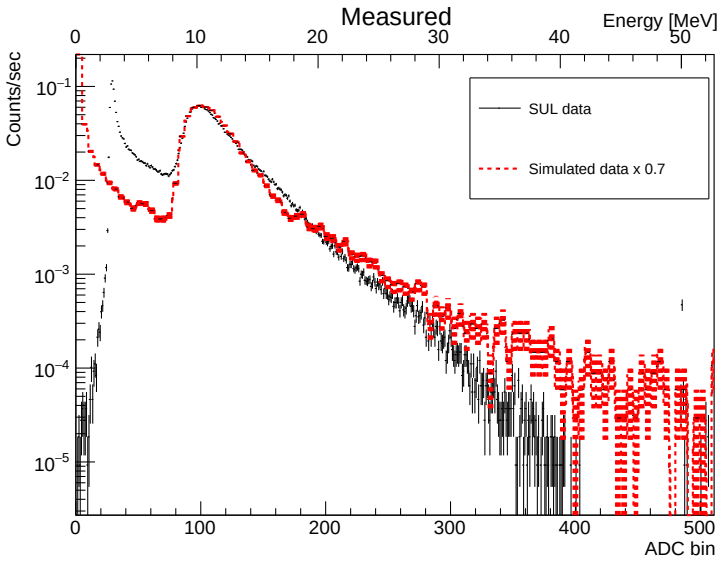

Figure 1: Validation of cosmic ray simulation with a PVT panel operated in the PNNL Shallow Underground Lab (∼19 m overburden). The main muon peak is best-fit by scaling the siulated rate by a factor of 0.7.

2.1.2 Ambient gamma environment

Estimating the ambient gamma flux followed several steps. First, we make the simplifying assumption that the gamma environment is dominated by the isotopes ^{40}K, ^{238}U, ^{232}Th (KUT) and their progeny in the concrete walls. As we will show below, this assumption agrees very well with the measured data.

The measured gamma-ray spectrum taken from an unshielded 140% relative efficiency ultra-low background high purity germanium (HPGe) detector sitting near the center of the lab away from any walls was taken in the SUL and analyzed using PeakEasy v4.86 to identify key terrestrial background gamma emitters. The most prominent isotopes identified were ^{40}K (K), ^{214}Pb (U), ^{214}Bi (U), ^{228}Ac (T), ^{212}Pb (T), ^{212}Bi (T), and ^{208}Tl (T) which accounted for 93.5% of the total terrestrial gamma background spectrum. These isotopes were simulated by distributing them uniformly throughout the concrete wall, and the characteristic gamma and x-ray emissions were generated using `GEANT4`'s radioactive decay module. The energy, position, and direction of each photon passing the surface of a 145 cm radius sphere centered on the HPGe were recorded.

As expected, Figure 2 shows that the measured flux is uniformly distributed along the azimuthal angles and polar angles, with no strong preference for emission from any direction nor any dependence on photon energy (i.e. lower-energy emitters like ^{212}Pb exhibit roughly the same distribution as a higher-energy emitter like ^{208}Tl). Likewise, Figure 3 shows that the measured flux is also isotropic to good approximation and with no dependence on photon energy. Because of this symmetry, we can "re-throw" the gamma flux originating from the walls both uniformly and isotropically from a simulated sphere inside the room and obtain similar results. These optimizations allow for significant speedup in simulations, as we can start the gamma-ray primaries for each simulation much closer to the volume of interest without re-transporting photons through the 1.2 m thick concrete wall upon every iteration on the shield design.

To determine the relative weights of the environmental sources, we compared the measurements taken with the HPGe detector in the SUL and determined the individual nuclide concentrations that minimized the chi-squared of the fit to the simulated HPGe response using CERN ROOT's Minuit2 solver [24], [25]. The HPGe (Mirion GC14022) detector used for these measurements was a p-type coaxial germanium detector with a vendor specified 140% relative efficiency at 1.33 MeV. Typically, due to uncertainties associated to the values of the detector parameters supplied by the vendor and/or

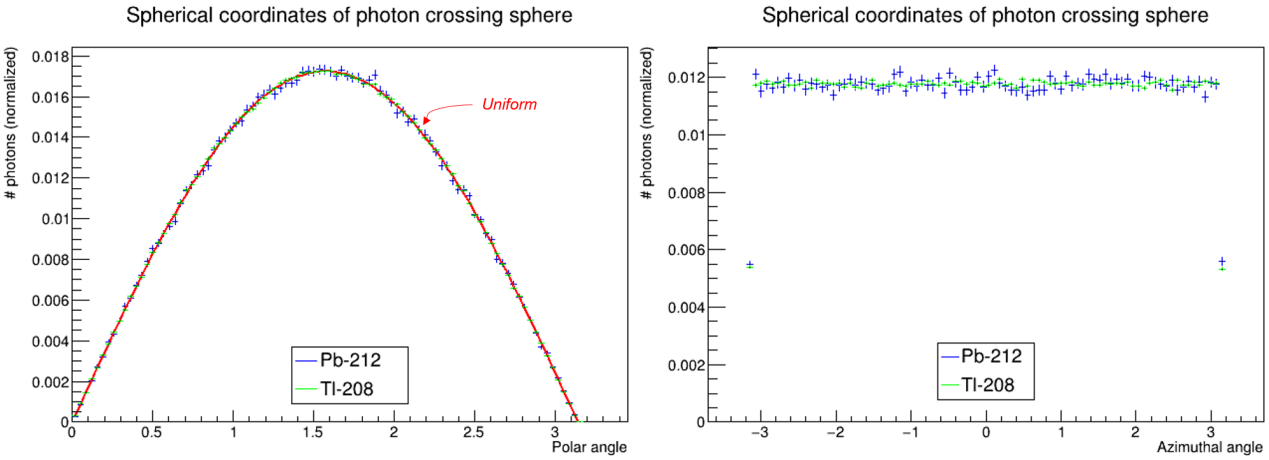

Figure 2: Positional distribution of gammas emitted by radioactive decay in the concrete walls as they cross a 145 cm radius sphere in spherical coordinates.

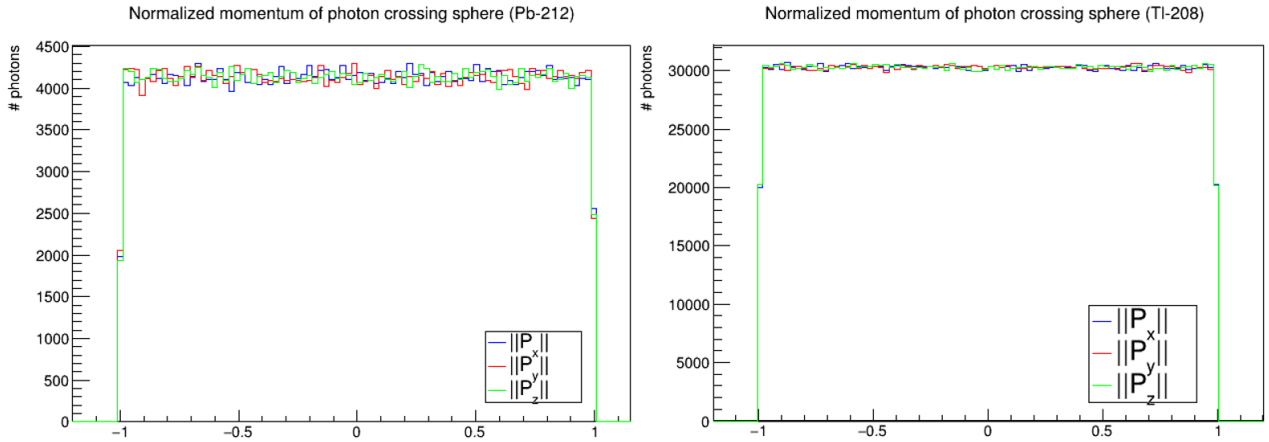

Figure 3: Angular distribution of gammas emitted by radioactive decay in the concrete walls as they cross a 145 cm radius sphere.

HPGe configuration	Vendor Specified	Optimized
Ge crystal		
Diameter	-	84 mm
Length	-	84 mm
Outer dead layer thickness	0.5 mm	1.2 mm
Inner dead layer thickness	0.3 μm	0.6 μm
Crystal holder		
Material	Cu	Cu
Thickness	-	7.5 mm
End cap		
Material	Al	Al
Thickness	-	0.5 mm
Diameter	108 mm	108 mm
Length	-	159 mm
Ge front to endcap distance	-	7.5 mm
Performance (at 1.33 MeV)	140%	136%

Table 1: Optimized and vendor provided parameters for Mirion GC14022 HPGe detector used in this work. The associated data is plotted in Figure 4.

aging and incomplete charge collection in the crystal, accurate simulation of a HPGe detector requires the optimization of several parameters. Of utmost importance, is the optimization of the dead layer thickness on the Ge crystal which significantly effects the HPGe response at low photon energies.

The final optimized HPGe parameters used for this simulation are shown in Table 1 and the final resultant simulated spectrum along with the measured HPGe spectrum is shown in Figure 4. The resulting total gamma flux spectrum is used as the starting point in simulations to evaluate the shielding efficacy.

2.2 Shield Design

Once we have determined the radiation environment in the underground laboratory, we must understand how that radiation interacts with a hypothetical superconducting qubit system. We simulate a very simple model of a dilution refrigerator (dil fridge) loosely based on a Bluefors LD system, the dimensions of which are detailed in Table 2. We use a 2×5×0.3 mm silicon wafer as a qubit substrate. Because the chance of incoming radiation interacting with such a small element is very low, in order to accumulate simulation statistics more quickly, we simulate a "quantum computing platform" with 144 such wafers. While representative of how superconducting qubit chips are operated in practice, for purposes of radiation transport simulation efficiency, groups of 9 wafers were placed together. Each group of nine wafers is placed inside a 3×3×2 cm copper box with 0.5 cm thick sides that would act as resonating cavity and RF shielding for typical microwave-addressed qubits. 16 of these units are attached to a 1/4" copper plate, 18 cm per side, hanging vertically from the dil fridge mixing chamber stage. Figure 5 shows the fridge and wafer layout.

For each radiation source (cosmic ray muons and ambient gammas), we calculate two quantities for the qubit wafers: interaction rate and absorbed dose per unit mass. For gammas, the interaction rate is calculated as the number of recorded interactions per primary photon, times the photon flux calculated in Section 2.1.2 times the area of the re-throwing surface. For cosmic rays, the interaction rate is the number of recorded interactions divided the livetime as reported by the CRY toolkit. The dose is equal to the interaction rate times the average energy deposited per interaction.

The radiation dose is the more important variable if the qubit interaction mechanism scales with the energy input, following the nonequilibrium quasiparticle density model in Vepsäläinen et. al.[26]. If, however, the qubit interaction is driven by prompt quasiparticle bursts coincident with radiation

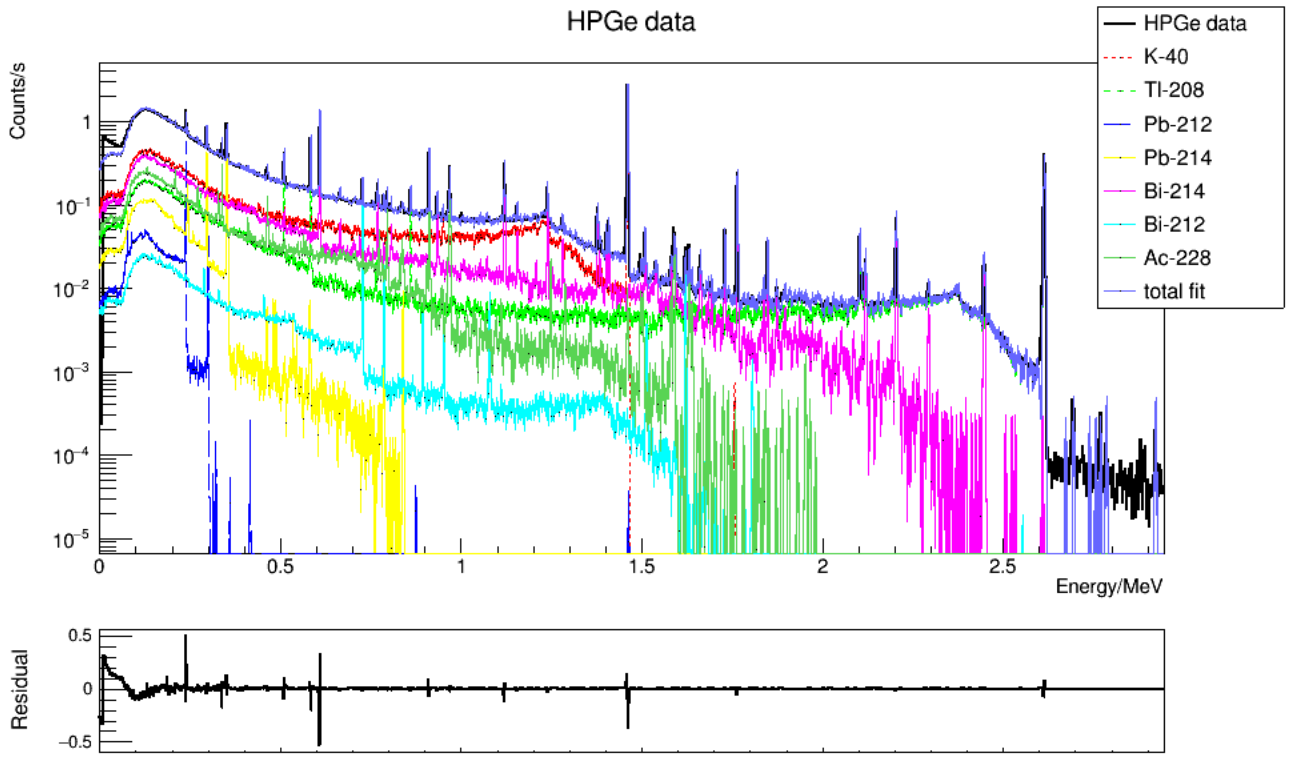

Figure 4: Comparison of measured terrestrial background spectra taken with HPGe along with the response to individual nuclides simulated and total simulated response.

Cooling stages

Stage	Vertical Offset	Radius	Thickness	Material
Vacuum Flange	0	261	12	stainless steel
50K	191	223.5	12	aluminum
4K	480	176	10	copper
Still	730	153	9	copper
Cold Plate	829	140	6	copper
Mixing Chamber	997	142.3	8	copper

Cans

Can	Vertical Offset	Radius	Height	Thickness	Material
Vacuum top	12	230	486	3.2	aluminum
Vacuum bottom	498	207.65	840	3.2	aluminum
50K top	203	204	286.5	1	aluminum
50K bottom	489.5	182	793	1	aluminum
4K	490	160	774	1.5	aluminum
Still	739	151.5	500	0.5	copper

Table 2: Dimensions of stages and cans for the simulated dilution refrigerator. All dimensions are in millimeters. All copper materials are assumed to be gold-plated. For simplicity in the simulation, gold-plated copper is modeled as copper with 0.1% bulk admixture of gold.

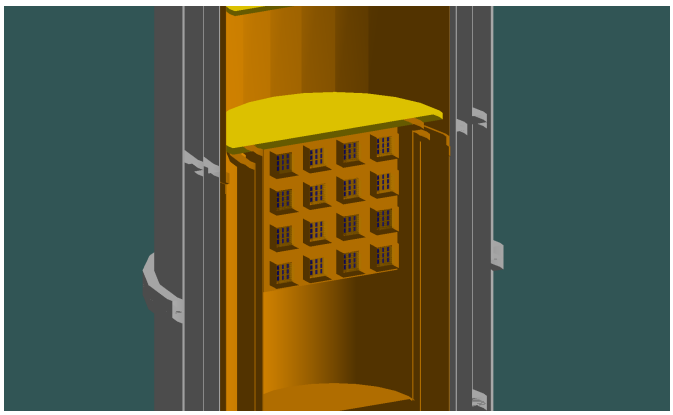

Figure 5: Cutaway view of the dilution refrigerator simulated in `GEANT4`. showing the quantum computing platform with 16 cavities each housing 9 silicon qubit wafers.

interactions [14], [16], the total amount of energy deposited may not be relevant as long as it is above some threshold. Cosmic rays, which interact more rarely but deposit more average energy, have a higher dose rate relative to gammas, and so in practice the shield design is driven by the interaction rate, since that produces the more stringent requirement. In other words, in an unshielded system, gamma rays account for the majority of the count rate, but a smaller fraction of the total dose, so the shield's effectiveness on dose rate hits diminishing returns sooner.

Simulations to guide the shield design followed three stages. First, we simulate cosmic rays and ambient gammas interacting with our dil fridge and qubit substrates without any shielding. This determines the required attenuation factor to bring the rate from gammas down to a fraction of that from cosmic rays. Then we add an idealized, hermetic lead shield around the dil fridge and vary the thickness until sufficient gamma-ray reduction is achieved. Finally, we add more realism to the shield, accounting for reductions in the shield's effectiveness due to e.g. mechanical supports and interferences, penetrations for cooling and signal lines, and gaps from finite mechanical tolerances. Results from this final stage inform the specifications for the shield's engineering design.

To simplify the large possible parameter space for the shield design, we assume the shield is built primarily from "standard" 2×4×8 inch bricks, This sets a natural step size for considering thickness variations. We also use this assumption to simplify modeling gaps in the shield to set extremely consertative tolerances. In the simulation, bricks in section are arranged with an edge parallel to the shield's thickness, such that any gaps between bricks become direct "holes" in the shield. We then add gaps of the specified tolerance around each individual brick and evaluate the effect. In the actual design, the bricks are arranged with overlapping gaps to prevent such direct lines of sight, and the only full gaps would be at the "seams" where movable sections meet. These are also mitigated in the design with stepped faces at the seams.

3 Results

3.1 Shield thickness

Figure 6 shows the simulated spectrum of ionizing interactions in the silicon substrates for cosmic rays and for the ambient gamma flux as a function of the thickness of an idealized hermetic lead shield. Table 3 summarizes the results. The "optimum" shield efficiency is not well defined: the total ionizing radiation interaction rate decreases with additional shielding, but with significantly diminishing returns as the residual gamma rate becomes much less than the cosmic ray rate. With 4 inches of lead shielding, the simulated gamma rate reaches about 10% of the cosmic ray rate, which we deem an acceptable compromise. For the 19m overburden we simulated, an additional 2 inches of shielding would reduce the *total* rate by roughly 9%. For deeper sites with more overburden, sufficient to reduce the cosmic

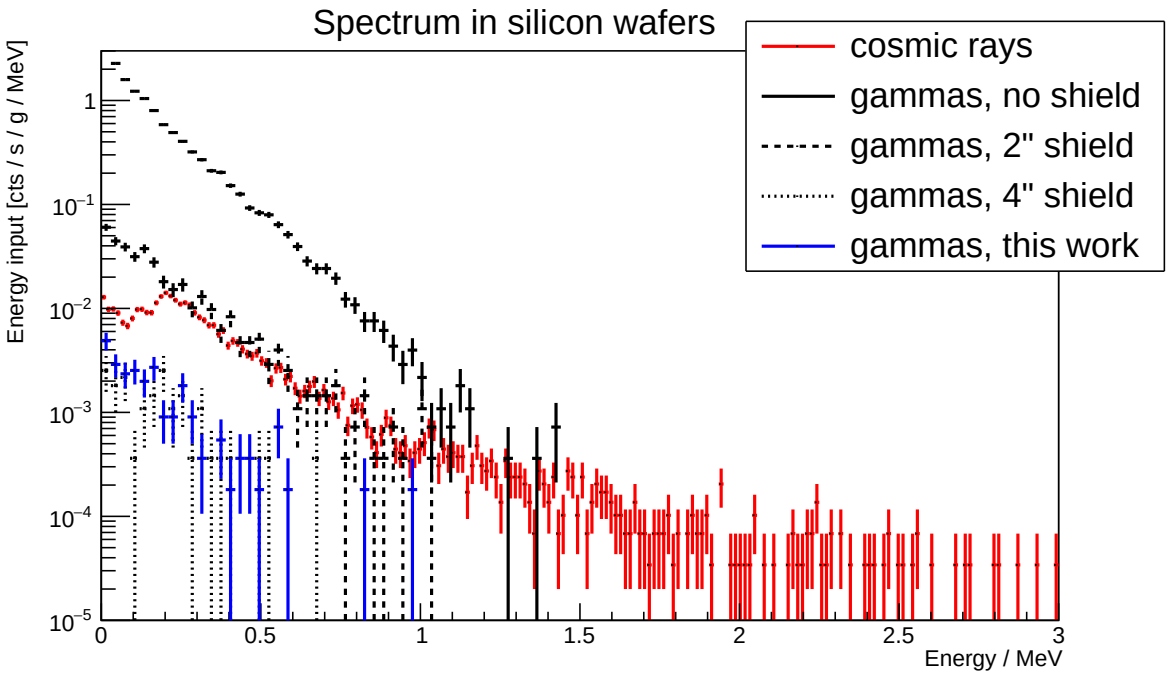

Figure 6: Simulated spectrum of ionizing interactions in the silicon substrates for cosmic rays and for the ambient gamma flux as a function of the thickness of an idealized hermetic lead shield, and for the shield with penetrations described in Section 3.2.

ray rate by an additional factor of ~ 10, additional shielding would also be warranted.

3.2 Mechanical design

Simulating a monolithic shield without penetrations, gaps, or imperfections is computationally convenient but unrealistic. This study took care to consider the mechanical limitations on shield coverage by including necessary perforations for the helium lines, experimental connections, mechanical maintenance, and loading limitations of the dil fridge. The shield design presented in Figure 8 accounts for these requirements. The shield is split into bottom and top sections to accommodate the section of frame from which the dilution refrigerator hangs. The shield is designed to be constructed from "standard" $2 \times 4 \times 8$ inch lead bricks, with a small number of half-size bricks. This allows the bricks to be stacked by hand during initial assembly. Once stacked, the bricks will be held in place by steel or aluminum sheets anchored to the frames.

The bottom shield forms a five-sided, open-topped "box," split into two sections: a single immovable wall, and a sliding "door" section for the bottom and remaining three sides that allows access to the refrigerator. When closed, the bottom section exterior dimensions are 32×34 inches by 52 inches high; each section is four inches thick. The fixed section is attached to and supported by the fridge frame. The whole assembly is shifted approximately two inches off the center of the fridge in the direction of the fixed section to allow access to the bolts on the top flange. The door section of the shield is held by a sturdy structure of aluminum extruded frame pieces, aluminum gussets, and aluminum plates. The door section contains an estimated 8100 pounds (3674 kg) of lead with a total estimated weight of 8820 pounds (4000 kg). The fixed section contains 2635 pounds (1195 kg) of lead and a total estimated weight of 3000 pounds (1360 kg). The door structure is mounted to a linear ball bearing system with a dynamic load capacity of 3800 pounds (1720 kg) that ride on two steel shafts mounted to support rails which are mounted to an aluminum plate. The door has six ball-bearing blocks to maintain a greater than 2.5 factor of safety. The door is moved by a motorized linear screw system to maintain minimal

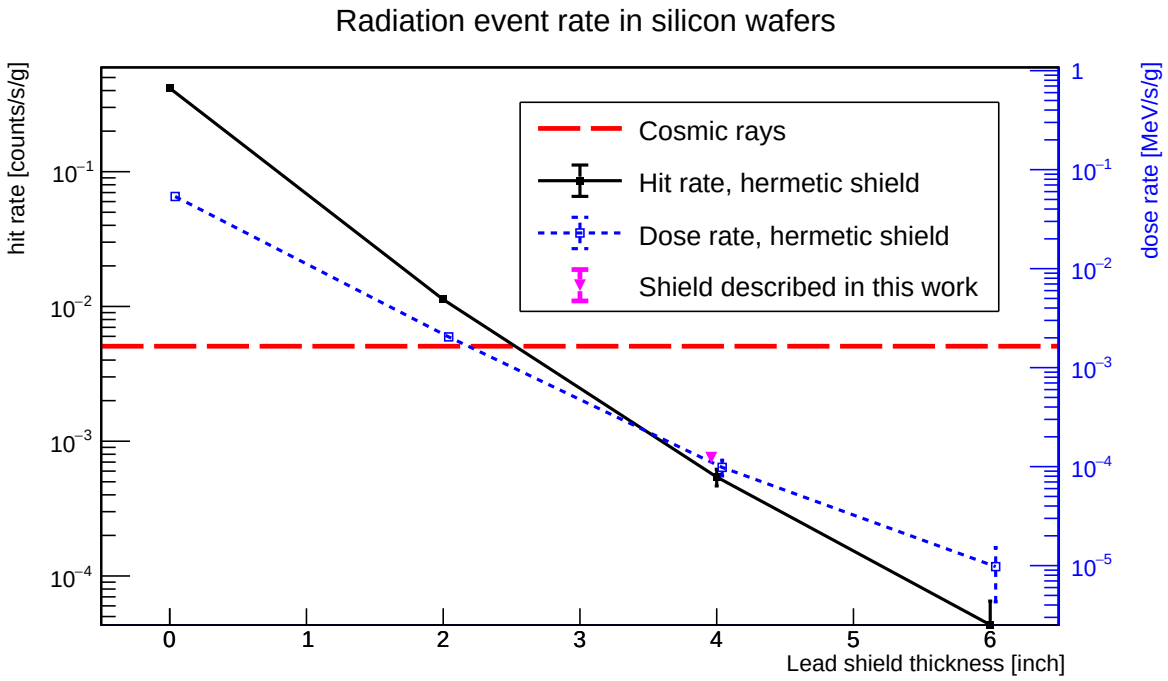

Figure 7: Simulated interaction rate (solid black, left axis) and dose rate (dashed blue, right axis) of ambient gammas as a function of shield thickness for an idealized hermetic lead shield. Cosmic rays (dashed red line) and the gamma rates for the shield described in Section 3.2 (magenta) are also shown. Points are slightly horizontally staggered to improve readablity. The vertical axes are arranged so that the cosmic ray and "this work" points are correct on both axes.

Shield configuration	Interaction rate (10^{-3} counts/s/g)	Dose rate (keV/s/g)
cosmic rays	5.07 $\pm$ 0.05	1.65 $\pm$ 0.02
gammas, no shield	417 $\pm$ 2	53.6 $\pm$ 0.4
gammas, 2" hermetic shield	11.3 $\pm$ 0.3	2.04 $\pm$ 0.09
gammas, 4" hermetic shield	0.54 $\pm$ 0.08	0.10 $\pm$ 0.02
gammas, 6" hermetic shield	0.04 $\pm$ 0.02	0.010 $\pm$ 0.005
gammas, this work	0.75 $\pm$ 0.06	0.12 $\pm$ 0.01
gammas, this work, 1 mm gaps	1.0 $\pm$ 0.1	0.14 $\pm$ 0.02

Table 3: Total simulated interaction rate and dose in silicon wafers from ambient gammas vs various lead shield designs. These data is plotted in Figure 6.

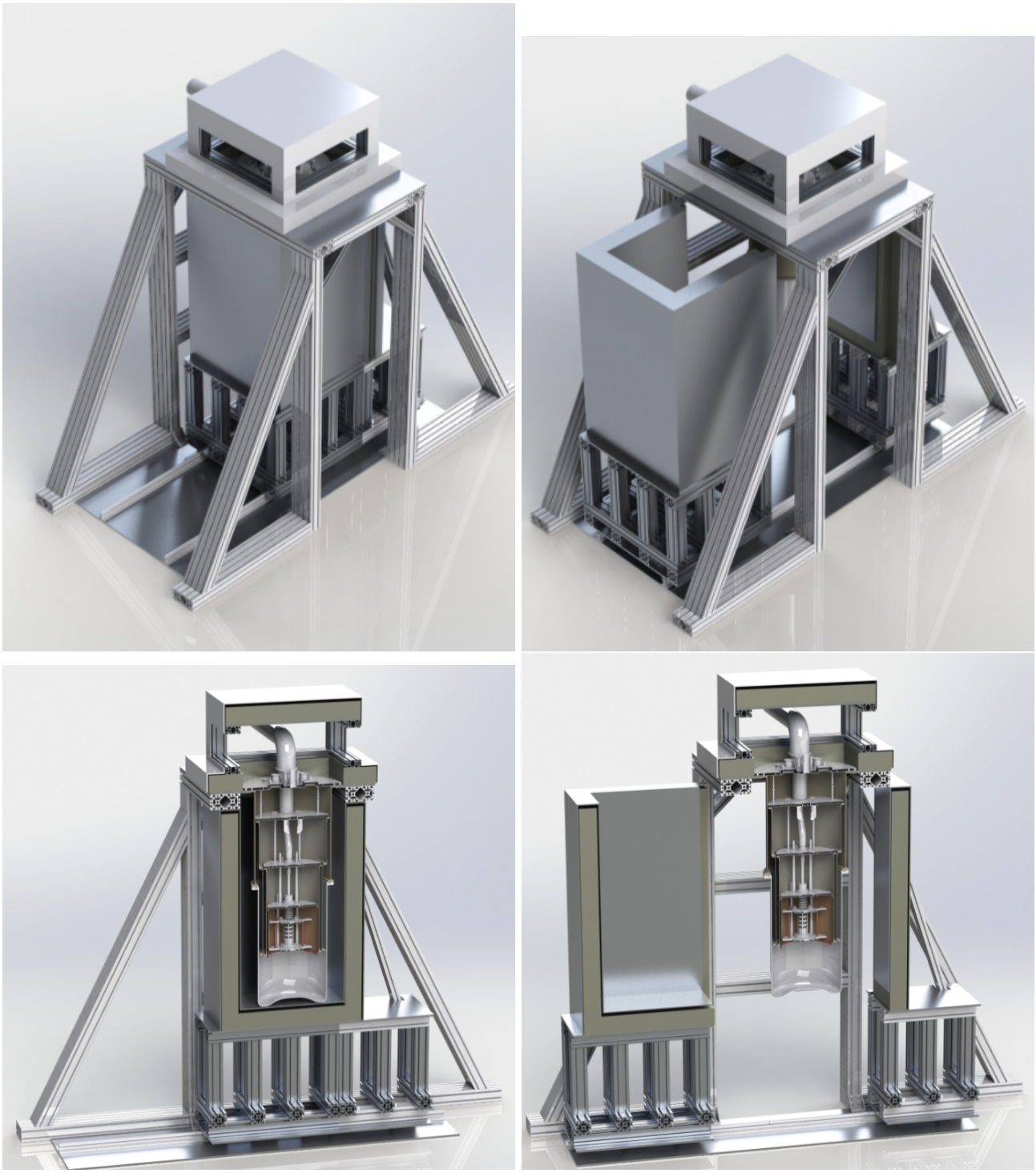

Figure 8: Renderings of the lead shield around the dilution refrigerator in closed (left) and open (right) configurations.

lateral momentum.

Shielding on top the frame is also divided into two sections, arranged in a square "top hat," with the 40×40 inch, 8 inch wide "brim" around the edge of the plate from which the fridge hangs, and the 32×32 inch top on a raised platform covering the center, overlapping the brim by four inches. The ~ 8 inch gap between the brim and top of the upper shield allow for plumbing and cabling. The fridge frame is reinforced to bear the additional lead weight. The arrangement of the top layers prevents any direct line-of-sight to the fridge experiment space. Supports are added to the legs of the frame and mounted to the floor or aluminum plated supporting the door sections of the shield. Estimated total weight of the cryostat (330 pounds or 150 kg), lead (4400 pounds or 2000 kg), external components (500 pounds or 227 kg), and internal components (300 pounds or 136 kg) is 5530 pounds (2513 kg). The frame is capable of supporting the estimated total weight of all estimated materials and components with a factor of safety well above 10. The frame is anchored to the laboratory wall (on the fixed bottom side) to stabilize the entire system in the event of seismic activity.

3.3 Tolerances

Table 3 lists the ionizing radiation interaction rate and dose for several shields considered in this work. The open sections of the shield described in Section 3.2 increase the interaction rate (absorbed dose) from ambient gammas by 40% (20%) as compared to an idealized hermetic 4" shield. Also shown is the effect of adding a 1 mm gap around every brick in the shield (with bricks place parallel to the shield's thickness), which would increase the interaction rate (dose) by another 30% (20%). Since even this extremely conservative estimate of the contribution from gaps is minimal, we are comfortable stating that a 1 mm ($\sim$1/16") tolerance for all gaps in the shield should be sufficient. The simulation can also be configured to evaluate specific gap tolerances, such as the "seam" where the two moving parts of the bottom part of the shield meet. However, since that particular seam does not have direct line-of-sight to the sensitive elements, we have not yet evaluated this requirement.

4 Discussion

An important consideration regarding the shield thickness is that we have assumed no active vetoing of the cosmic ray muons. Low background counting systems such as HPGe detectors often employ such vetoes (typically large plastic scintillator panels) to reduce cosmic ray-induced backgrounds by at least an order of magnitude. Some types of superconducting sensors may benefit from such a veto, but it is not clear whether qubits or other quantum instruments can. For example, if cosmic ray muons generate prompt quasiparticle bursts [14], this will lead to coincident decoherence in a quantum device. In this case, a muon veto may be able to reject bad data points from some kinds of quantum sensors. Alternatively, it could be that the overall decoherence rate is the important factor, in which case flagging the time of decoherence with the veto may not have any practical benefit. Moreover, if the energy input from cosmic rays leads to an excess steady-state quasiparticle population [26], decoherence might not be coincident with muon events, in which case a muon veto will again not be effective.

If the cosmic ray muon rate can be lowered, either by operating in a deeper site or by the use of a muon veto, the shield would need to be made thicker to keep the ambient gamma rate below the cosmic rays. However, this may not be as simple as increasing the thickness with the design we have presented. First, as the shield gets thicker, the rate from gammas entering the shield through penetrations without direct line-of-sight to the qubits becomes more important. Additional "shadow" shielding may be needed to reduce this effect. Second, internal sources also become relatively more important. At some point, there are no additional gains to be had from a thicker shield unless the radioactivity of all components inside the dilution fridge is controlled first. Some of these sources are considered in Section C. As Table 5 shows, we expect the rate from sources of radiation inside the fridge to be roughly half of the residual external rate with the current shield design, so improved shielding will again have limited returns without redesigning the fridge to use low radioactivity components. Finally, there are additional engineering considerations, particularly for the upper shield sections that are held up by the vendor support frame, which might need to be reinforced if significant additional weight is added.

References

[1] J. Preskill, "Quantum Computing in the NISQ era and beyond," *Quantum*, vol. 2, p. 79, Aug. 2018. DOI: 10.22331/q-2018-08-06-79.

[2] Douglas Beck *et al.*, *Nuclear Physics and Quantum Information Science*, 2019. [Online]. Available: https://science.osti.gov/-/media/np/pdf/Reports/NSAC_QIS_Report.pdf?la=en&hash=91703C70429F2B7D634CBC10573079858926141D (visited on 11/09/2020).

[3] I. C. Cloët *et al.*, "Opportunities for Nuclear Physics & Quantum Information Science," *arXiv:1903.05453 [hep-ex, physics:nucl-ex, physics:nucl-th, physics:physics, physics:quant-ph]*, Jul. 2019. arXiv: 1903.05453 [hep-ex, physics:nucl-ex, physics:nucl-th, physics:physics, physics:quant-ph]. [Online]. Available: http://arxiv.org/abs/1903.05453 (visited on 12/12/2020).

[4] J. Carlson, D. J. Dean, M. Hjorth-Jensen, D. Kaplan, J. Preskill, K. Roche, M. J. Savage, and M. Troyer, "Quantum Computing for Theoretical Nuclear Physics, A White Paper prepared for the U.S. Department of Energy, Office of Science, Office of Nuclear Physics," Tech. Rep. 1631143, Jan. 2018. DOI: 10.2172/1631143.

[5] C. L. Degen, F. Reinhard, and P. Cappellaro, "Quantum sensing," *Reviews of Modern Physics*, vol. 89, no. 3, p. 035 002, Jul. 2017. DOI: 10.1103/RevModPhys.89.035002.

[6] F. Hassler, A. R. Akhmerov, and C. W. J. Beenakker, "The top-transmon: A hybrid superconducting qubit for parity-protected quantum computation," *New J. Phys.*, vol. 13, no. 9, p. 095 004, Sep. 2011, ISSN: 1367-2630. DOI: 10.1088/1367-2630/13/9/095004.

[7] W. D. Oliver and P. B. Welander, "Materials in superconducting quantum bits," *MRS Bulletin*, vol. 38, no. 10, pp. 816–825, Oct. 2013, ISSN: 0883-7694, 1938-1425. DOI: 10.1557/mrs.2013.229.

[8] M. Kjaergaard, M. E. Schwartz, J. Braumüller, P. Krantz, J. I.-J. Wang, S. Gustavsson, and W. D. Oliver, "Superconducting Qubits: Current State of Play," *Annual Review of Condensed Matter Physics*, vol. 11, no. 1, pp. 369–395, 2020. DOI: 10.1146/annurev-conmatphys-031119-050605.

[9] X. Y. Jin *et al.*, "Thermal and Residual Excited-State Population in a 3D Transmon Qubit," *Physical Review Letters*, vol. 114, no. 24, p. 240 501, Jun. 2015. DOI: 10.1103/PhysRevLett.114.240501.

[10] K. Serniak, M. Hays, G. de Lange, S. Diamond, S. Shankar, L. D. Burkhart, L. Frunzio, M. Houzet, and M. H. Devoret, "Hot Nonequilibrium Quasiparticles in Transmon Qubits," *Physical Review Letters*, vol. 121, no. 15, p. 157 701, Oct. 2018. DOI: 10.1103/PhysRevLett.121.157701.

[11] L. Grünhaupt, N. Maleeva, S. T. Skacel, M. Calvo, F. Levy-Bertrand, A. V. Ustinov, H. Rotzinger, A. Monfardini, G. Catelani, and I. M. Pop, "Loss Mechanisms and Quasiparticle Dynamics in Superconducting Microwave Resonators Made of Thin-Film Granular Aluminum," *Physical Review Letters*, vol. 121, no. 11, p. 117 001, Sep. 2018. DOI: 10.1103/PhysRevLett.121.117001.

[12] A. Bespalov, M. Houzet, J. S. Meyer, and Y. V. Nazarov, "Theoretical Model to Explain Excess of Quasiparticles in Superconductors," *Physical Review Letters*, vol. 117, no. 11, p. 117 002, Sep. 2016. DOI: 10.1103/PhysRevLett.117.117002.

[13] A. P. Vepsäläinen *et al.*, "Impact of ionizing radiation on superconducting qubit coherence," *Nature*, vol. 584, no. 7822, pp. 551–556, Aug. 2020, ISSN: 1476-4687. DOI: 10.1038/s41586-020-2619-8.

[14] L. Cardani *et al.*, "Reducing the impact of radioactivity on quantum circuits in a deep-underground facility," *Nature Communications*, vol. 12, no. 1, p. 2733, May 2021, ISSN: 2041-1723. DOI: 10.1038/s41467-021-23032-z.

[15] C. D. Wilen *et al.*, "Correlated charge noise and relaxation errors in superconducting qubits," *Nature*, vol. 594, no. 7863, pp. 369–373, Jun. 2021, ISSN: 1476-4687. DOI: 10.1038/s41586-021-03557-5.

[16] M. McEwen *et al.*, "Resolving catastrophic error bursts from cosmic rays in large arrays of superconducting qubits," *arXiv:2104.05219 [quant-ph]*, Apr. 2021. arXiv: 2104.05219 [quant-ph]. [Online]. Available: http://arxiv.org/abs/2104.05219 (visited on 04/27/2021).

[17] P. W. Shor, "Scheme for reducing decoherence in quantum computer memory," *Physical Review A*, vol. 52, no. 4, R2493–R2496, Oct. 1995. DOI: 10.1103/PhysRevA.52.R2493.

[18] A. M. Steane, "Error Correcting Codes in Quantum Theory," *Physical Review Letters*, vol. 77, no. 5, pp. 793–797, Jul. 1996. DOI: 10.1103/PhysRevLett.77.793.

[19] R. Klesse and S. Frank, "Quantum Error Correction in Spatially Correlated Quantum Noise," *Physical Review Letters*, vol. 95, no. 23, p. 230 503, Nov. 2005. DOI: 10.1103/PhysRevLett.95.230503.

[20] A. G. Fowler, M. Mariantoni, J. M. Martinis, and A. N. Cleland, "Surface codes: Towards practical large-scale quantum computation," *Physical Review A*, vol. 86, no. 3, p. 032 324, Sep. 2012. DOI: 10.1103/PhysRevA.86.032324.

[21] J. L. Orrell and B. Loer, "Sensor-Assisted Fault Mitigation in Quantum Computation," *Physical Review Applied*, vol. 16, no. 2, p. 024 025, Aug. 2021. DOI: 10.1103/PhysRevApplied.16.024025.

[22] C. E. Aalseth *et al.*, "A shallow underground laboratory for low-background radiation measurements and materials development," *Review of Scientific Instruments*, vol. 83, no. 11, p. 113 503, Nov. 2012, ISSN: 0034-6748. DOI: 10.1063/1.4761923.

[23] S. Agostinelli *et al.*, "Geant4—a simulation toolkit," *Nucl. Instr. Meth. A*, vol. 506, no. 3, pp. 250–303, Jul. 2003, ISSN: 0168-9002. DOI: 10.1016/S0168-9002(03)01368-8.

[24] M. Hatlo, F. James, P. Mato, L. Moneta, M. Winkler, and A. Zsenei, "Developments of mathematical software libraries for the LHC experiments," *IEEE Trans. Nucl. Sci.*, vol. 52, pp. 2818–2822, 2005. DOI: 10.1109/TNS.2005.860152.

[25] R. Brun and F. Rademakers, "ROOT: An object oriented data analysis framework," *Nucl. Instrum. Meth. A*, vol. 389, M. Werlen and D. Perret-Gallix, Eds., pp. 81–86, 1997. DOI: 10.1016/S0168-9002(97)00048-X.

[26] A. P. Vepsäläinen *et al.*, "Impact of ionizing radiation on superconducting qubit coherence," *Nature*, vol. 584, no. 7822, pp. 551–556, Aug. 2020, ISSN: 1476-4687. DOI: 10.1038/s41586-020-2619-8.

[27] G. Battistoni, C. Bloise, A. Ferrari, M. Monteno, V. Patera, and E. Scapparone, "Monte carlo simulation of underground muon events in a finite size detector," *Astroparticle Physics*, vol. 7, no. 1, pp. 101–108, Jun. 1997, ISSN: 09276505. DOI: 10.1016/S0927-6505(97)00010-8. [Online]. Available: https://linkinghub.elsevier.com/retrieve/pii/S0927650597000108.

[28] E. Aprile *et al.*, "Material screening and selection for XENON100," *Astroparticle Physics*, vol. 35, no. 2, pp. 43–49, Sep. 2011.

[29] D. S. Leonard *et al.*, "Systematic study of trace radioactive impurities in candidate construction materials for EXO-200," *Nucl. Instr. Meth. A*, vol. 591, no. 3, pp. 490–509, Jul. 2008, ISSN: 0168-9002. DOI: 10.1016/j.nima.2008.03.001.

[30] N. Abgrall *et al.*, "The Majorana Demonstrator radioassay program," *Nucl. Instr. Meth. A*, vol. 828, pp. 22–36, Aug. 2016, ISSN: 0168-9002. DOI: 10.1016/j.nima.2016.04.070.

A Muon Flux Validation

In order to validate the rate normalization obtained from `CRY`, we compare the results of a simulation to measurements. A $76 \times 76 \times 5$ cm^3 PVT scintillator panel, typical for muon veto systems, was added to the simulation. Primary particles were simulated using the `CRY` toolkit, and the resulting energy deposition spectra in the PVT panel were normalized to counts per second using the livetime as reported by `CRY`. This spectrum is compared to ADC measurements for a panel of those same dimensions. For all simulations, the PVT panel is placed in an $8 \times 8 \times 4$ m^3 room 2.4 m from the floor.

For the surface comparison, the room was surrounded by 1 m concrete walls. Cosmic ray muon primaries are generated at the edge of the "ceiling" (2.6 m from the PVT panel) in a 20×20 m^2 plane. Figure 9 shows a fit of the resulting simulation without variance reduction to 17.2 hours of data measured in the basement of the the RPL building on the PNNL campus. The only free parameters in the fit are a linear scale factor to convert energy deposited to recorded ADC counts and a scaling amplitude. The fit was performed over the range 4500-20000 ADC counts (approximately 8.9-39 MeV). The best fit is obtained by scaling the simulated spectrum by 1.257 ± 0.003, indicating the `CRY` is under-reporting the rate (or equivalently over-reporting the livetime) by about 25%. Slightly better fit results can be obtained by allowing for non-linear energy conversion or spectral broadening due to finite resolution, but these do not have significant impact on the amplitude scaling and were not applied here. The under-coverage of the simulation in the high energy region above ∼40 MeV most likely indicates that 20 m is an insufficient extent for primary generation at surface, as the highest energies will be from muons traversing the PVT at large oblique angles, i.e. originating far from vertically above. However, this high energy region represents only about 0.7% of the total spectrum.

For the shallow overburden validation, the walls were 1.2 m of concrete, and an overburden of calcium carbonate (limestone or chalk) with a density of 2.8 g/cm^3 extending 19 m above and to the sides of the concrete, as shown in Figure 10. Cosmic ray muon primaries are generated just at the top of the overburden (22 m from the PVT panel) from a 38×38 m^2 plane. Figure 1 shows a fit of the simulated data without variance reduction to 30 hours of data measured in the PNNL Shallow Underground Lab. The fit was performed over the range 75-250 ADC counts (approximately 7.7-26 MeV). The best fit is obtained by scaling the simulated spectrum by 0.705 ± 0.003.

The effect here is opposite to that at surface: the simulated rate is higher than measured, and there is more relative weight in the simulated high-energy tail. Overall the fit is much poorer than surface. In addition to any errors present in the primary particle production, the underground spectrum will also be influenced by inaccuracies in our definition of the overburden, which is approximate at best. In particular, there are likely differences in the material composition, density, and shape at surface (berms, etc). Nevertheless, the simulation largely agrees with measured data both at surface and underground within $\sim 30\%$.

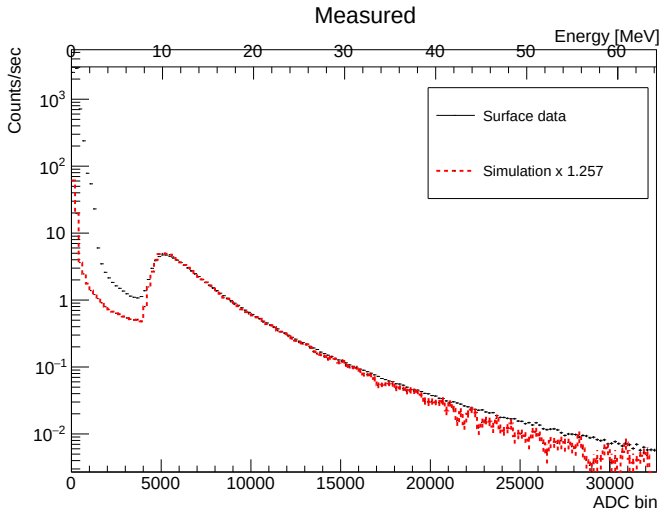

Figure 9: Validation of cosmic ray simulation with a PVT panel operated at surface.

B Variance Reduction Techniques

Monte Carlo methods are, inherently, computationally and time intensive; so much so that obtaining statistically relevant results with singular compute nodes within days to weeks is challenging. This complication has been encountered in other cosmic background simulations; thus, highlighting the need to accelerate the simulation process. Variance reduction is the most common method of mitigating this problem.

Two methods of variance reduction were explored: 1) proposed by Battistoni in [27] which makes use of repeated geometries to increase the tally count-rate, and 2) source biasing. Figure 10 depicts the model configuration of a dilution fridge housing sensitive instruments within a concrete shell and 19 m soil overburden.

The muon source-term relative to a small object can be treated as an anisotropic plane source. As noted by Battistoni and Bielajew, repeated structures at a constant altitude are effectively equivalent because of the translation invariance of the problem. No impact on the angular or energy dependence of the incident particle tally was observed using this method.

The second method used, source biasing, makes use of a maximum radial acceptance criteria whereby the direction of primaries at birth, $\hat{u}$, must be directed towards the tally volume. Using the center point of the tally volume, v_t, initial starting point of the primary, v_p, and a radial point perpendicular to the vector between the center of the tally volume and initial primary position $\hat{u_t} = v_t - v_p$ at a user specified distance, the maximum possible angle difference between the direction of the primary and $\hat{u_t}$ is computed as θ_a along with the angle between $\hat{u}$ and $\hat{u_t}$ as θ_u. Only particles with $\theta_h \leq \theta_a$ are emitted and tracked. Unlike Battistoni's method, this technique was expected to reduce the number of low energy events. This bias was verified by applying the variance reduction technique to the PVT panel validation case simulations.

The radial acceptance range was evaluated at 1, 2, 3, 4 and ∞ m. The comparison of results is provided in Figure 11. Virtually no impact to the muon peak or high-energy tail was observed but a significant reduction in low energy events (80% reduction in the lowest energy bin) was observed using a 1 m acceptance criteria applied to 76 cm square PVT panel, as expected. This discrepancy was quickly reduced, however, by expanding the radial acceptance window; the 4 m window achieving 80% of bin value observed with an open acceptance window in the lowest energy bin. An improvement in events processed per CPU hr of a factor of $\approx$170 was observed with a 1 m acceptance window and reducing inversely to the square of radius. An improvement of $\approx$10 was achieved using an acceptance window of 4 m.

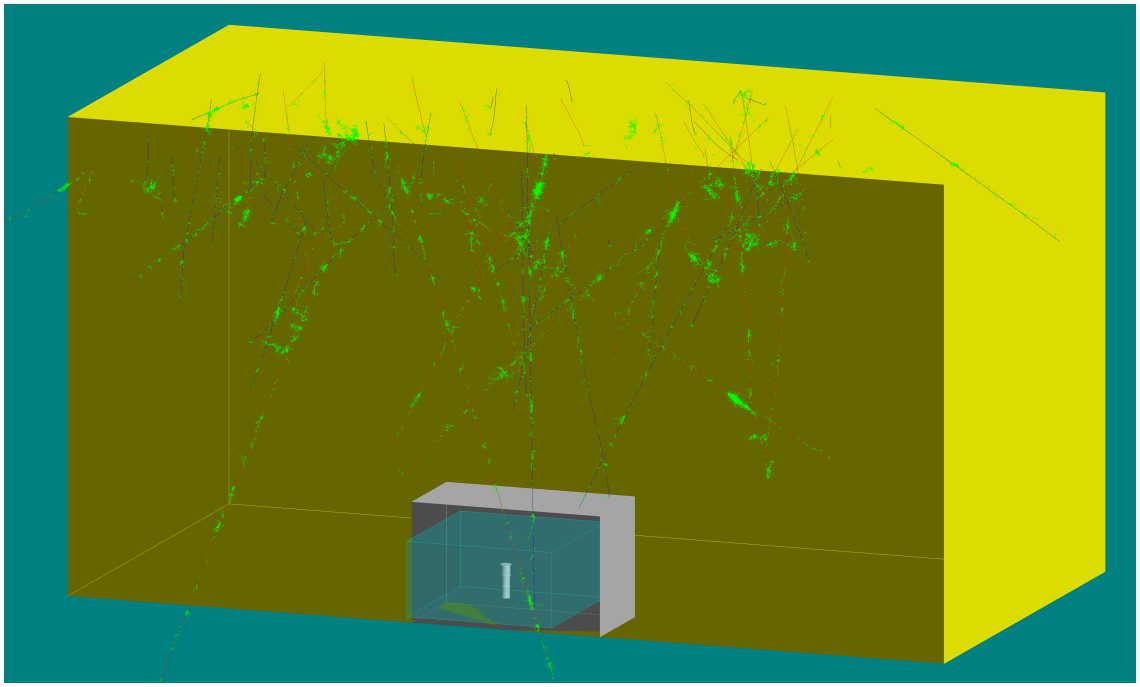

Figure 10: CAD rendering of dilution fridge within a concrete cavity beneath a 19 m overburden.

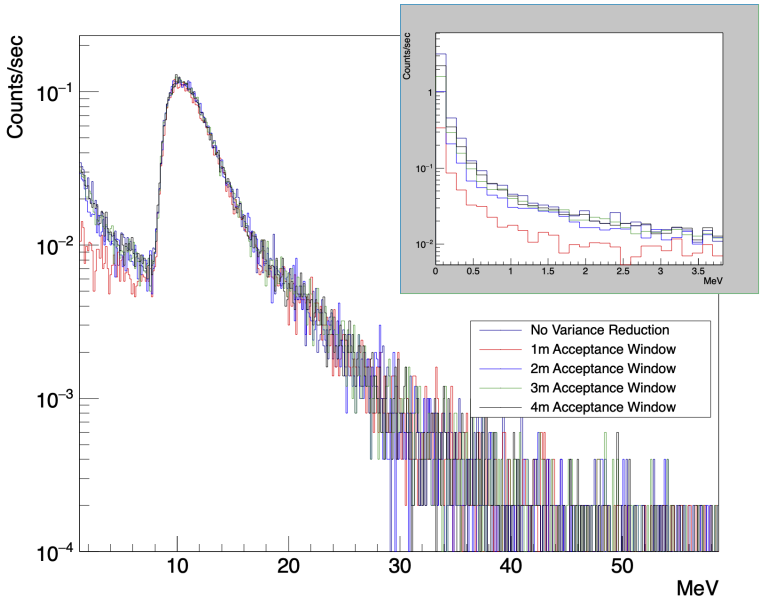

Figure 11: Comparison of the simulated muon spectrum as a function of the acceptance radius cut employed for variance reduction. A 1 meter cut shows significant divergence from the uncut spectrum at low energies.

Contaminant	Level in material (mBq/kg) copper	steel	aluminum	gold
^{238}U	11	130	66	74.4
^{235}U	0.47	2	2.64	3
^{232}Th	0.37	2.4	200	18.5
^{210}Pb	40	–	–	–
^{137}Cs	0.14	0.9	–	–
^{60}Co	0.24	8.5	–	–
^{40}K	1.3	10	2100	146

Table 4: Radio-contaminant levels used to normalize the simulated dose per disintegration estimated using GEANT4. References: copper [28], stainless steel [28], aluminum [29], and gold [29], [30].

C Sources of Internal Dose

The components within a dilution refrigerator do contain trace quantities of primordial radioactivity, predominantly from ^{40}K, $^{238/235}$U, and ^{232}Th (KUT). In addition to these environmental contaminants modern sources of steel and copper have ^{60}Co contamination both from nuclear testing and blast furnace liners.

As noted in the cosmogenic and terrestrial background evaluations, the estimated energy deposition or dose rates within the qubits is anticipated to be on the order of 10^{-3} MeV/kg-sec. This factor is expected to dominate the energy dose exposure of the qubits; however, the magnitude of the dose-rate from internal sources is not clearly defined. The decay of known radio-contaminants uniformly distributed within components of the fridge were simulated using GEANT4 to estimate the energy spectrum of the absorbed dose for each isotope. The associated energy deposition spectrum was then normalized to reported contamination levels provided by radiopurity.org. The highest possible contaminant levels were assumed and are provided in Table 4.

A range of materials may be considered as common materials used in a dilution refrigerator. These materials include: stainless steel, copper, brass, bronze, Kapton, teflon, delrin, viton, indium vacuum seals, silver solder, vacuum grease, Cu-Ni supports, ceramics, Be-Cu pins etc.... However, not all components generate enough radiation in proximity of the qubits to impact them. More to the point, the arrangement of subsidiary materials will be highly experiment-dependent. Here we consider only the elements of the dil fridge itself (cooling stages and cans) and the isotopes listed in Table 4. For each of the components listed in Table 5, we simulated decays of each isotope uniformly throughout the component's volume, record the counts and energy deposited in the qubit wafers, and normalize by the assumed mass and contamination level.

The estimated rate and dose from internal sources is reported in Table 5. Two features are worth exploration. First, the total estimated rate is approximately 5% of the residual rate from external gammas with the shield in place. This indicates that further increasing the lead shield efficiency from the design presented in this work will have limited effect. A more detailed study of the internal sources would be required. However, the largest single contributor to the induced rate is the RF cavities (the small copper boxes that house 9 silicon wafers in the simulated geometry). This is unsurprising as that is the material closest to the qubit wafers. This suggests that further reducing the internal rate could be attained by replacing the cavities with higher-purity copper screened for radioactive contamination, and possible deploying additional shielding inside the fridge.

Component	Material	Mass (kg)	Interaction rate (counts/s/g)	Dose rate (MeV/s/g)
Vacuum flange	steel	21	$8 \pm 3 \times 10^{-7}$	$7 \pm 3 \times 10^{-8}$
50K stage	aluminum	15	$7 \pm 3 \times 10^{-6}$	$5 \pm 2 \times 10^{-7}$
4K stage	aluminum	8.7	$7 \pm 1 \times 10^{-6}$	$6 \pm 2 \times 10^{-7}$
Still	copper	5.9	$5.0 \pm 0.4 \times 10^{-7}$	$1.6 \pm 0.3 \times 10^{-8}$
Cold Plate	copper	3.3	$6.3 \pm 0.3 \times 10^{-7}$	$1.9 \pm 0.2 \times 10^{-8}$
Mixing Chamber	copper	4.6	$6.7 \pm 0.1 \times 10^{-6}$	$8.6 \pm 0.3 \times 10^{-7}$
Vacuum chamber	aluminum	22	$1.13 \pm 0.08 \times 10^{-4}$	$1.3 \pm 0.1 \times 10^{-5}$
50K can	aluminum	6.7	$5.5 \pm 0.3 \times 10^{-6}$	$7.7 \pm 0.6 \times 10^{-6}$
4K can	aluminum	3.7	$5.4 \pm 0.3 \times 10^{-5}$	$5.7 \pm 0.4 \times 10^{-6}$
Still can	copper	5.66	$4.2 \pm 0.1 \times 10^{-6}$	$1.34 \pm 0.08 \times 10^{-7}$
gold plating	gold	0.22	$2.53 \pm 0.06 \times 10^{-6}$	$2.2 \pm 0.1 \times 10^{-7}$
RF cavity	copper	2	$1.82 \pm 0.01 \times 10^{-4}$	$2.10 \pm 0.01 \times 10^{-5}$
Total			$4.48 \pm 0.10 \times 10^{-4}$	$5.1 \pm 0.2 \times 10^{-5}$
ambient gammas (shielded)			$7.5 \pm 0.6 \times 10^{-4}$	$1.2 \pm 0.1 \times 10^{-4}$
cosmic rays			$5.07 \pm 0.05 \times 10^{-3}$	$1.65 \pm 0.02 \times 10^{-3}$

Table 5: Simulated interaction rate and dose from some components inside the dilution refrigerator. The estimated residual rates from cosmic rays in the SUL and external gammas passing through the shield are included for comparison. Included uncertainties are statistical only.

Pacific Northwest National Laboratory

902 Battelle Boulevard
P.O. Box 999
Richland, WA 99354
1-888-375-PNNL (7665)

www.pnnl.gov